JGR Space Physics

RESEARCH ARTICLE
10.1029/2022JA030262

Key Points:

- Coincidence of the Electromagnetic Ion Cyclotron wave observation is studied using conjugate space [Geostationary Operational Environment Satellite (GOES) 13] and ground (SNK ground magnetometer) observations
- The Coincidence of the waves is primarily dominated by wave power and duration
- The high-frequency wave filtering is complicated by both magnetospheric and ionospheric wave propagation

Correspondence to:
S.-J. Noh,
sjnoh@njit.edu

Citation:
Noh, S.-J., Kim, H., Lessard, M., Engebretson, M., Pilipenko, V., Kim, E.-H., et al. (2022). Statistical study of EMIC wave propagation using space-ground conjugate observations. *Journal of Geophysical Research: Space Physics*, *127*, e2022JA030262. https://doi.org/10.1029/2022JA030262

Received 5 JAN 2022
Accepted 23 JUN 2022

Statistical Study of EMIC Wave Propagation Using Space-Ground Conjugate Observations

Sung-Jun Noh[1], Hyomin Kim[1], Marc Lessard[2], Mark Engebretson[3], Vyacheslav Pilipenko[4], Eun-Hwa Kim[5], Jay Johnson[6], Ilya Kuzichev[1,4], and Michelle Salzano[2]

[1]Center for Solar-Terrestrial Research, New Jersey Institute of Technology, Newark, NJ, USA, [2]University of New Hampshire, Durham, NH, USA, [3]Augsburg University, Minneapolis, MN, USA, [4]Space Research Institute RAS, Moscow, Russia, [5]Princeton Plasma Physics Laboratory, Princeton University, Princeton, NJ, USA, [6]Andrews University, Berrien Springs, MI, USA

Abstract In the present study, we explore the observational characteristics of Electromagnetic Ion Cyclotron (EMIC) wave propagation from the source region to the ground. We use magnetometers aboard Geostationary Operational Environment Satellite (GOES) 13, the geosynchronous orbit satellite at 75°W, and at Sanikiluaq ground station (SNK, 79.14°W and 56.32°N in geographic coordinates, and $L \sim 6.0$ in a dipole magnetic field) which is located in northern Canada. Using these magnetically conjugate observatories, simultaneous EMIC wave observations are carried out. We found a total of 295 coincident and 248 non-coincident EMIC wave events between GOES 13 and the SNK station. Our statistical analysis reveals that the coincident events are predominantly observed on the dayside. The wave normal angles are slightly higher for the non-coincident events than for coincident events. However, the coincidence of the waves is mostly governed by the intensity and duration of the wave. This is confirmed by the geomagnetic environment which shows higher auroral electrojet (AE) and Kp indices for the coincident events. We also found that some events show high-frequency ($f > 0.4$ Hz) wave filtering. The statistics of the high-frequency filtered and non-filtered wave events show that there are clear magnetic local time (MLT) and F10.7 index differences between the two groups, as well as in ionospheric electron density measurements. In addition, we also found differences in the wave properties which possibly indicate that the propagation in the magnetosphere also plays an important role in the wave filtering.

1. Introduction

Electromagnetic Ion Cyclotron (EMIC) waves are the ion-scale waves that are known to be generated with left-handed polarization with respect to the background magnetic field (L-mode) and typically propagate with a group velocity aligned with the background magnetic field. It is also known that the polarization and the direction of the propagation of the wave can change during their propagation. EMIC waves are frequently observed in the Earth's magnetosphere and are generally accepted as significant contributors to the loss of both the radiation belt electrons as well as ring current ions via wave-particle interactions (Chen et al., 2011; Cornwall et al., 1970; Jordanova et al., 2008; Kim et al., 2021; Meredith et al., 2003; Miyoshi et al., 2008; Ni et al., 2015; Saikin et al., 2015; Summers & Thorne, 2003; Thorne & Kennel, 1971). EMIC waves at geosynchronous orbit are known to predominantly occur near the magnetic equator from noon to the dusk sector (Clausen et al., 2011). Conditions in this L range are favorable for EMIC wave excitation where the plasma density is high and the intensity of the magnetic field is low, such as in a plasmaspheric plume or near the plasmapause (Fraser & Nguyen, 2001; Summers, 2005). Since the dispersion relation for EMIC waves is complicated by the presence of the heavier ions such as He^+ or O^+, their propagation is thought to be confined within the source region to mid-latitudes and cannot propagate through the stopband where the wave is evanescent. Historically, however, there have been many studies that report ground observations in the Pc 1 – 2 (0.1–5 Hz) frequency range which corresponds to the typical frequency of EMIC waves near the outer radiation belt region (Arnoldy et al., 1979; Engebretson et al., 2018; Hayakawa et al., 1992; Kim et al., 2010, 2011; Ludlow et al., 1989; Usanova et al., 2010).

A number of models and ground-based observations showed that EMIC waves injected into the ionosphere can be ducted in the F region then significantly propagate in the horizontal direction, consequently spreading over a wider area than the original beam incident region (Fujita & Tamao, 1988; Greifinger & Greifinger, 1968; Kim et al., 2010, 2011; Mann et al., 2014). While the ducting in the ionosphere gives us more chance to observe EMIC

waves on the ground, it also makes specifying the beam incident location at the top of the ionosphere complicated. Besides that, the ionosphere has intrinsic resonant frequencies (e.g., ionospheric Alfven resonator—IAR) which may influence the propagation (Fedorov et al., 2018).

Lessard et al. (2015) reported 5 years of ground observations of EMIC waves at Halley station ($L = 4.6$). They found the number of EMIC wave events increased by ∼60% at the end of 2012 compared to the solar minimum in 2009. A systematic variation of the frequency of EMIC waves according to the solar cycle was also reported in their work. They suggested that the frequency variation is possibly due to plasmapause erosion and the change of heavy ions content near the generation region. They also found a seasonal dependence of the wave frequency that shows predominant observation of higher frequency ($f > 0.4$ Hz) waves in the winter season when the ionospheric density is relatively low. In addition, Upadhyay et al. (2020) reported a statistical study of ground EMIC wave observations at the Maitri station ($L = 5.0$). They found a higher occurrence rate of the EMIC wave event during the winter season than the summer season, although they did not incorporate the frequency dependence of the wave.

There has been a significant number of space-ground conjugate observations of EMIC waves (Braysy & Mursula, 2001; Engebretson et al., 2018; Ludlow et al., 1989, 1991; Perraut et al., 1984; Usanova et al., 2008, 2010). Braysy and Mursula (2001) surveyed conjugate observations of EMIC waves between the Polar satellite and the Sondankyla ground station. Thanks to the highly eccentric orbit of the Polar satellite and a small local time difference between the Polar and Sondankyla stations, they could limit the effects of horizontal ducting in the longitudinal direction. They found that 75% of the EMIC wave events are observed simultaneously in space and on the ground. Half of the simultaneously observed EMIC waves are within the conjunction box (within ±1.5 magnetic local time (MLT and ±5° invariant latitude). They also found one-third of the H^+-band waves are not observed on the ground while only one He^+-band wave is not observed on the ground.

The presence of the heavy ions in the magnetosphere forms stopbands in the dispersion relation of L-mode EMIC waves. This inhibits the wave propagation to higher latitudes as the wave frequency normalized by the local hydrogen gyrofrequency decreases with propagation to higher latitudes, thus the wave inevitably encounters the stopband during their propagation. However, such L-mode waves can penetrate into the ground through polarization reversal, mode conversion, and tunneling (Hu et al., 2010; Johnson & Cheng, 1999; Johnson et al., 1995; Kim & Johnson, 2016). Using a 2D full-wave simulation code, Kim and Johnson (2016) found that propagation of the EMIC wave can be sensitive to the wave normal angle near the source region (i.e., magnetic equator). EMIC waves launched at the magnetic equator with oblique wave normal angle can easily reach higher magnetic latitudes through mode conversion and polarization reversal.

The propagation in the ionosphere also has been studied. Fedorov et al. (2018) numerically modeled the propagation characteristics of the Pc1 wave through the ionosphere. They compared the transmission of the Pc1 wave with the perpendicular wavelength of 100 km in summer between day and night conditions. The transmission windows have oscillatory signatures depending on the frequency owing to the resonant features of the ionosphere. The transmission rate rapidly changes with the frequency below 1 Hz. The frequency of the transmission window significantly depends on the distance from the beam incident location and the ionospheric condition.

In the present study, we statistically investigate the EMIC wave properties and related geomagnetic conditions using simultaneous observation from the source region at the magnetic equator to the ground using the Geostationary Operational Environment Satellite (GOES) 13 ($L = 6.6$ in dipole and 75°W in geographic coordinates) and the ground magnetometer installed at Sanikiluaq (SNK, $L = 6.0$ in dipole, 79.14°W, and 56.32°N in geographic coordinates). We first describe the data set that we use in this study in Section 2. The statistical comparison of coincident and non-coincident wave events is introduced in Section 3. In Section 4, we discuss high-frequency wave filtering which demonstrates more complicated propagation characteristics. Then we conclude the study with summary and discussions in Section 5.

2. Data and Methodology

2.1. Space and Ground Observations

GOES 13, a geosynchronous satellite located at 75°W, was launched in May 2006. Its mission was discontinued in December 2017 and was transferred to GOES 16. The Space Environment Monitor (SEM) aboard the GOES

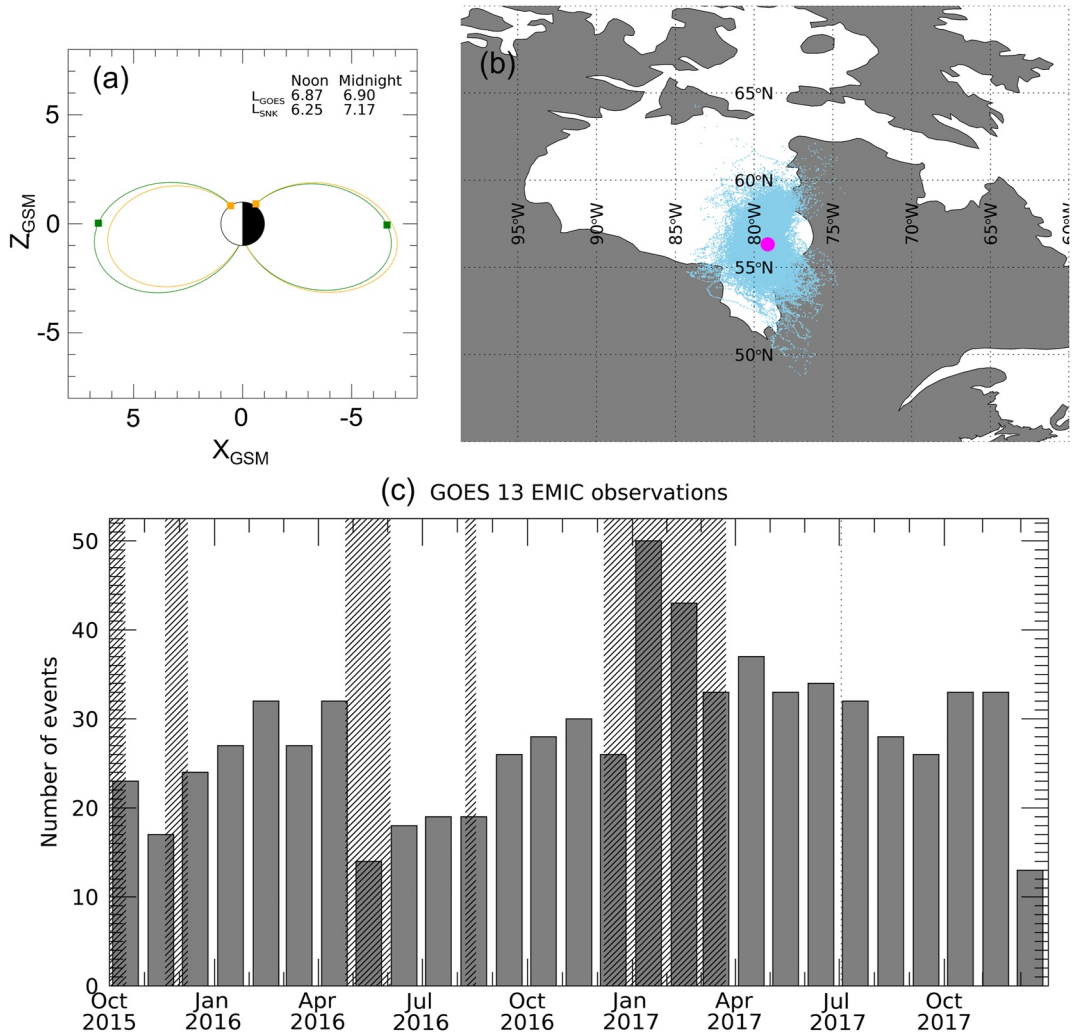

Figure 1. (a) The magnetic field line configurations traced from both Geostationary Operational Environment Satellite (GOES 13) (green) and SNK station (orange) at equinox assuming quiet solar wind conditions. (b) Ground footprints of GOES 13 (blue dots) and the Sanikiluaq ground magnetometer (magenta circle) from October 2015 to December 2017. (c) Monthly distribution of Electromagnetic Ion Cyclotron (EMIC) waves observed by GOES 13. The shaded areas indicate the time interval the SNK instrument was not operational.

13 is a set of various instruments designed to observe the near-Earth space environment (Singer et al., 1996). The fluxgate magnetometer (MAG) in the SEM measures the 3-dimensional vector magnetic field with a sampling rate of 512 ms.

The induction coil magnetometer installed at Sanikiluaq (SNK, 56.32°N and 79.14°W, geographic), Canada, was developed by the University of New Hampshire. It is now part of the Magnetic Induction Coil Array (MICA, PI: Marc Lessard). The magnetometer consists of two axial components which measure the time variation of the magnetic field (dB/dt) horizontal to the ground. The X-axis of the magnetometer points to the north magnetic pole and the Y-axis (orthogonal to X) is eastward. The noise level of the magnetometer is 0.07 pT/Hz2 at 1 Hz with a sampling rate of 10 Hz (Shin et al., 2016). The SNK magnetometer was operational from October 2015 to September 2018. In this study, the data used were collected from October 2015 to December 2017, when both GOES 13 and the SNK magnetometer were in operation.

The advantage of using GOES 13 and the SNK magnetometer is that they are magnetically conjugate. Moreover, thanks to the geostationary orbit of GOES 13, the conjunction is always valid throughout the entire mission period. Figure 1a shows the noon and midnight magnetic field line passing both GOES 13 (green) and SNK

(orange) locations obtained from the TS04D model (Tsyganenko & Sitnov, 2005) with quiet solar wind conditions at the equinox. From the survey of the L shell difference between GOES 13 and SNK for the entire period, we found that 90% out of over 2 years of their operation are within $|\Delta L| < 1$. Figure 1b shows the ground location of the SNK magnetometer and the ground footprints of GOES 13 during the entire operation. The footprints of the GOES 13 satellite are mostly located near SNK, within ±5° in the geographic latitude and longitude.

2.2. Wave Detection

In order to identify EMIC wave events from GOES 13 measurements, we use the method as follows. First, the three-axis magnetic field data from the MAG instrument in NEP (eastward, earthward, and poleward) coordinates are transformed to a field-aligned coordinate system (FAC) such that Z points in the fieldline direction, X = Z × N (N: eastward), and Y completes the right-handed coordinate system. The local mean-field is determined by taking a sliding average of the data with a time interval of 10 min. Then we subtract the mean-field from each of the original X, Y, and Z components to obtain the fluctuation component of the magnetic field in each direction. Second, the time domain data are transformed to the frequency domain by using a short-term Fast Fourier transform. We set the time window to 5 min with overlaps of ∼50% (2.5 min). Once the spectral matrix, which is composed of real parts of the coefficients, is determined, we calculate the power spectral density (hereafter PSD) by taking a summation of diagonal terms of the spectral matrix.

Individual wave events are identified based on the automated wave detection algorithm developed by Bortnik et al. (2007) and confirmed by visual inspection. To follow Bortnik et al.'s algorithm, first, we take the median values of PSD over 1 day (one complete orbit) at each frequency and subtract them from the original PSD spectrum for all time segments. Here we take the base 10 logarithm to both the median and original PSD for both quantities. Second, the subtracted PSD is smoothed with a five points time window (∼10 min) and we take the subtracted PSD value above 1 as a wave event. Any wave events that occurred within 5 min of the adjacent event are treated as one event. Finally, to make our definition of an EMIC wave stringent, we exclude any broadband spikes based on visual inspection and limit our event selection to those which are well organized along ion gyrofrequencies. With this scheme, we have identified 757 events during the overlapped period of observation between GOES 13 and SNK. Figure 1c shows the monthly distribution of identified EMIC waves observed by GOES 13. There were some intervals when SNK observations were not available that are shaded in Figure 1c. Excluding the events during non-operating periods of SNK, 560 events out of the 757 events are used for the present statistical study.

3. Simultaneous Observations of EMIC Waves—Coincident, Non-Coincident Events

To investigate the basic characteristics of EMIC wave propagation, we first separate the entire wave event into two groups based on whether waves are simultaneously observed by both GOES 13 and at SNK (hereafter, a coincident event), or observed only by GOES 13 but not on the ground (hereafter, a non-coincident event). Note that this classification is based on the GOES 13 observation to focus on the EMIC wave propagation from space to the ground. Figure 2 shows examples of a coincident event (top) and a non-coincident event (bottom). For the coincident event, a series of EMIC waves occurred on 30 October 2015, from 17:00 to 24:00 UT. The observed waves are well below and organized along the local He^+ gyrofrequency which is denoted by gray lines. During the same time interval, the SNK ground magnetometer observes similar wave structures over time and frequency as well. On the other hand, the event that occurred on 5 March 2016, lasted ∼1.25 hr (from 18:10 to 19:25, at a similar local time to the above coincident event) in the He^+-band which is the frequency band between the local He^+ and O^+ gyrofrequency. This event was not observed on the ground.

For the entire observation period, we found 295 coincident events and 248 non-coincident events. We exclude 17 events out of 560 events since the field line tracing is not available for these events due to a lack of input parameters (see Table 1).

In this section, based on the classification of the coincident and non-coincident events, statistics of the spatial distributions (L and MLT), geomagnetic activities (auroral electrojet (AE) index, Sym-H, Kp index, F10.7 index, and solar wind dynamic pressure), and the wave properties (amplitude, duration, ellipticity, and wave normal angle) are investigated. For the investigation of the geomagnetic activity dependence, a maximum value within 2 hr before the wave onset to the end of the event is selected for the AE, Kp, solar wind dynamic pressure, and

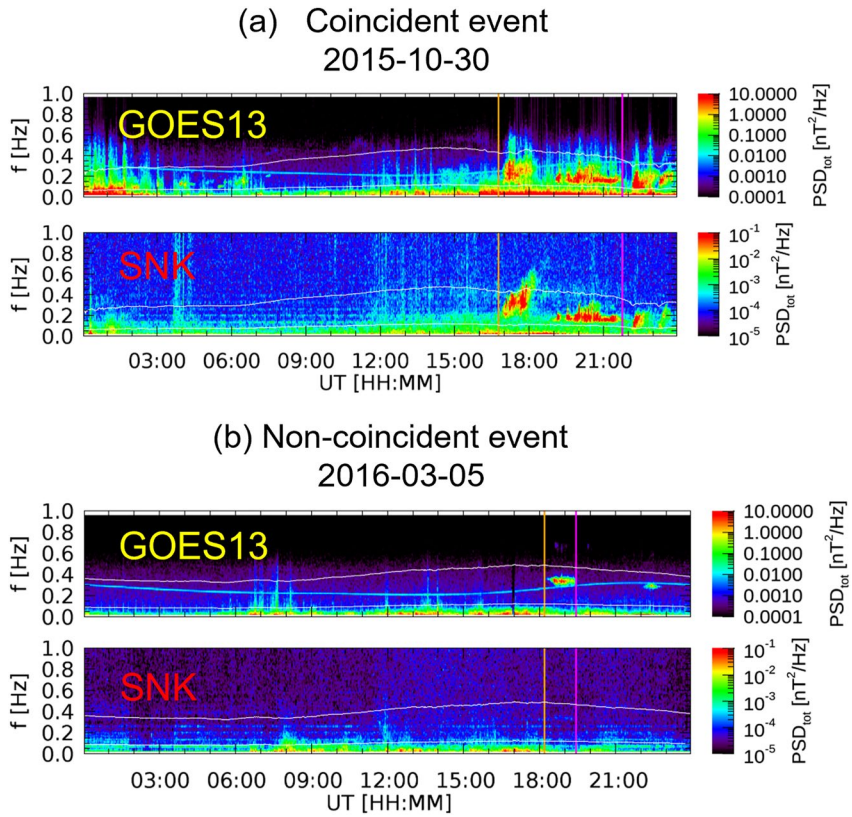

Figure 2. Example spectrograms of (a) a coincident event and (b) a non-coincident event. The upper panels show the Geostationary Operational Environment Satellite (GOES) 13 observations and the bottom panels show the SNK observations. The gray lines in each panel indicate the local He^+ gyrofrequency at the GOES 13 location.

F10.7, and the minimum value within 2 hr is selected for the Sym-H. We use the international geomagnetic reference field (IGRF-12) model (Thébault et al., 2015) as an internal magnetic field and the TS04D model as an external magnetic field model for the estimation of *L* shell.

Figures 3a and 3b show the *L* and MLT distributions of EMIC waves observed by GOES 13, respectively. The statistical difference in *L* shell between the coincident and the non-coincident groups is not significant although the non-coincident events tend to have higher *L* values. This is related to the MLT distribution. Notably, the coincident group is mostly confined within the noon to the dusk sector, while the non-coincident events are distributed evenly compare to the coincident events. Since the orbit of GOES 13 is geophysically fixed at geosynchronous orbit, the *L* shell of GOES 13 is lower than that of the SNK station on the nightside due to the stretched field line but is higher on the dayside.

Table 1
The Number of Events Used in This Study

Total number of events observed by GOES 13	The number of events during periods of SNK operation	The number of events when the field line tracing is possible	
757	560	543	
		Coincident	Non-Coincident
		295	248
		Filtered	Non-Filtered
		30	32

We investigated the *L* shell difference (ΔL) between GOES 13 and SNK. 88% out of the entire EMIC wave events have $|\Delta L| < 1$, and 62% events have $|\Delta L| < 0.5$. Blum et al. (2017) suggested that the typical scale size of EMIC waves is 0.5 Re in the Van Allen Probes orbit. Considering GOES 13 and SNK are located at higher *L* shells than the Van Allen Probes and the wave signal can be horizontally spread due to the ducting in the ionosphere, most of the EMIC waves are observed by GOES 13 are geomagnetically close enough to be observed by the SNK station.

We also investigated the ground distance between the footprint of GOES 13 and SNK. The determination of the footprint of GOES 13 depends heavily on the magnetic field model. That might introduce a systematic uncertainty for the footprint location. For example, the distance between modeled ground

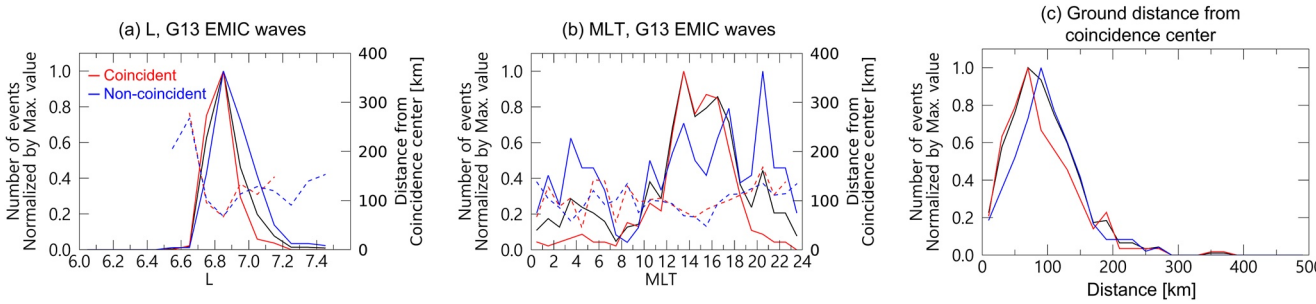

Figure 3. Histograms of (a) L, (b) magnetic local time (MLT), and (c) ground distance from coincidence center distributions of the Electromagnetic Ion Cyclotron (EMIC) wave. The red traces indicate the coincident events, the blue traces indicate non-coincident events, and the black traces indicate total events. The dashed traces in panels (a and b) indicate the average distance between the coincidence center and the footprints of Geostationary Operational Environment Satellite (GOES) 13 for each bin. The L and MLT values are estimated based on the location of GOES 13.

footprints and the SNK station shows statistically farther distances for coincident events than for non-coincident events (not shown). This should not be seen as a contradictory result because the real position of the GOES footprint might be different from the modeled estimation. To overcome this difficulty, we employed the concept of a coincidence center which is an average location of coincident events. This is based on the assumption that the coincidence of the wave could be affected by the distance between the two observations. Figure 3c shows the ground distance from the coincidence center to the footprint of GOES 13 for coincident and non-coincident events. Although the ground distances are farther for the non-coincident events than coincident events, the average distance is somewhat similar, 91 km for coincident events and 99 km for non-coincident events. The result indicates that, for the given spatial scales between GOES 13 and SNK station, magnetic conjugacy is not a major factor controlling the coincidence of waves. To avoid any statistical bias due to the relative distance between the two observations, the average distance for each bin in each figure is plotted throughout Section 3.

The statistics for geomagnetic activity are shown in Figure 4. The statistics of the AE index and Kp index indicate that coincident events are more likely to occur due to strong substorm activity in the magnetosphere. However, the SYM-H, F10.7 indices, and the solar wind dynamic pressure show similar statistics between the coincident and non-coincident groups. This implies that the coincidence of the wave is closely related to certain geomagnetic activity (in particular, substorms) but does not highly depend on all possible triggers that can excite the EMIC wave, such as geomagnetic storms and dayside magnetic field compressions.

In Figure 5, the statistics for the wave properties are introduced. It seems clear that the duration of the wave events is longer for the coincident group than for the non-coincident group. The average duration of each event is 91.8 and 52.4 min for the coincident and non-coincident groups, respectively. Similarly, the average wave amplitude (Bw) is statistically higher for the coincident group than for the non-coincident group. This result is consistent with Clausen et al. (2011) in which they show a positive correlation between the Kp index and the EMIC wave amplitude observed by the geosynchronous satellite. The statistics of the wave duration and amplitude indicate that the longer and the stronger wave activity has more chance to be observed on the ground. The ellipticity is slightly more L-mode for the coincident group than the non-coincident group although the overall ellipticities are low in both groups, and are mostly linear for the non-coincident group. The wave normal angle, which is the angle between the wave vector and the background magnetic field, is slightly different between the two groups, that is the non-coincident group has a higher wave normal angle than the coincident group (Figure 5d). Moreover, the fraction of highly oblique wave events (wave normal angle >50°) is much higher for the non-coincident group than for the coincident group although the majority of the wave normal angle for both groups is still small (<20°).

4. High-Frequency Wave Filtering

Among the coincident event group, we found that some wave events with multi-band signatures in the GOES 13 data show only partial frequency components on the ground. We call this type of event the "filtered event." The frequency filtering mostly occurred at higher frequencies. We empirically specified the cutoff frequency to be 0.4 Hz. Although the cutoff frequency is somehow similar to the local He^+ gyrofrequency, we determined not

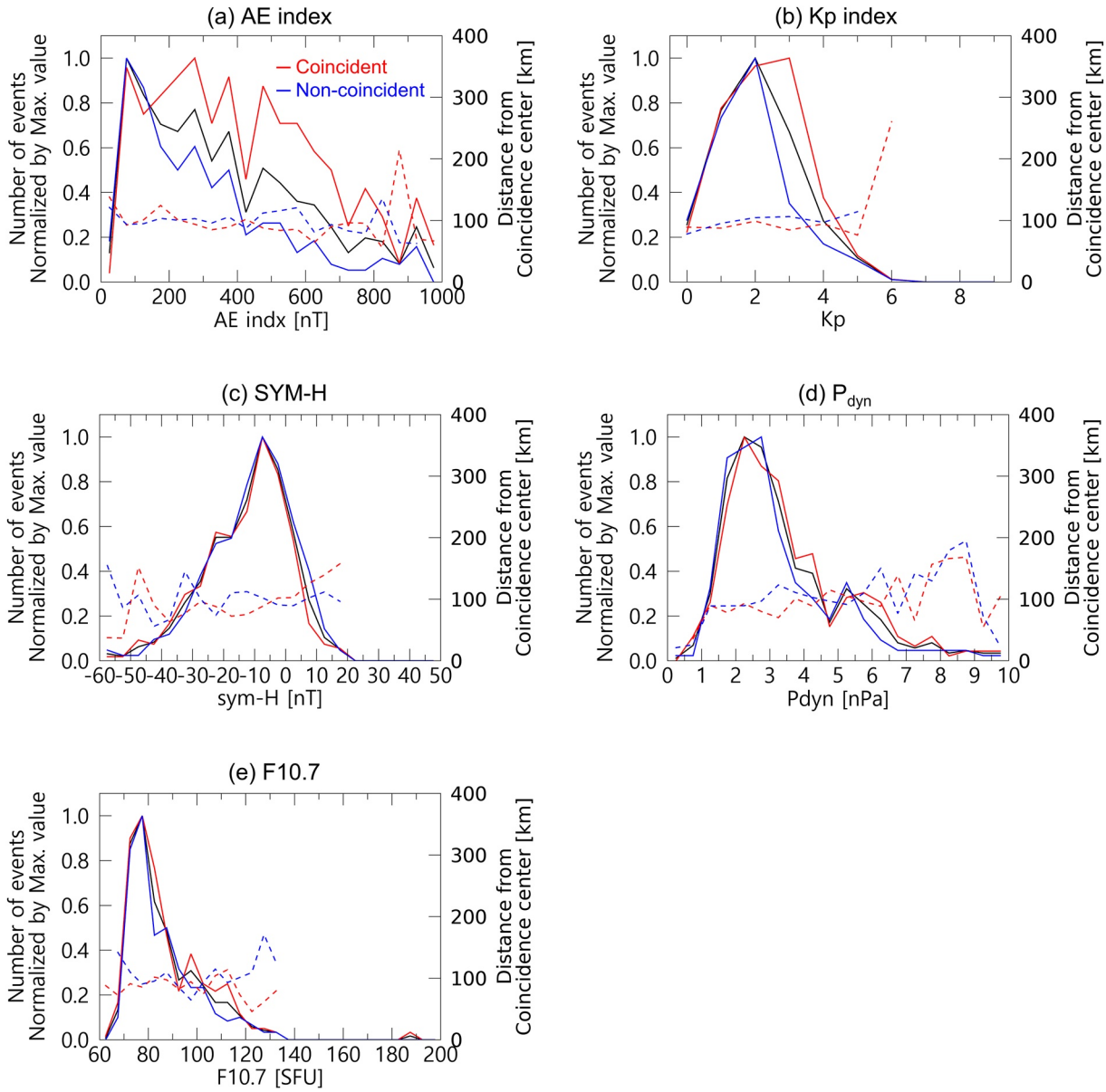

Figure 4. Histograms of the geomagnetic activity during coincident (red), non-coincident (blue) events, and total (black) events, (a) auroral electrojet (AE) index, (b) Kp index, (c) Sym-H, (d) solar wind dynamic pressure, and (e) F10.7 index.

to specify this to local f_{cHe+} at geosynchronous orbit since it is not clear whether the high-frequency filtering is due to a magnetospheric effect near the source region or an ionospheric effect since both effects more efficiently affect higher frequency components. For a comparison to the filtered event, we selected wave events that showed high-frequency wave components both in space and on the ground. We name this type of event a "non-filtered event." Since the sensitivities of the magnetometers aboard the GOES 13 and at the SNK station are different, there is a possibility that the high-frequency part of the spectrum can be buried by the noise level of the ground measurement. In order to prevent this artificial frequency filtering, we compare the power spectral density of the high-frequency (>0.4 Hz) and low-frequency (≤0.4 Hz) spectrum and calculate the ratio of the spectrum between space and ground for both bands ($R = PSD_{space}/PSD_{ground}$). Then we choose the events which have a comparable power ratio between the high-frequency and low-frequency or the R_{high} is higher than R_{low}. This is a strict criterion because the fluxgate magnetometer on GOES 13 adopts a five-pole Butterworth lowpass filter at 0.5 Hz which may suppress the PSD above and around 0.5 Hz at GOES 13 (Singer et al., 1996). Out of 295 total coincident events, we found 30 filtered events that met the noise ratio threshold. For the comparison to the filtered event,

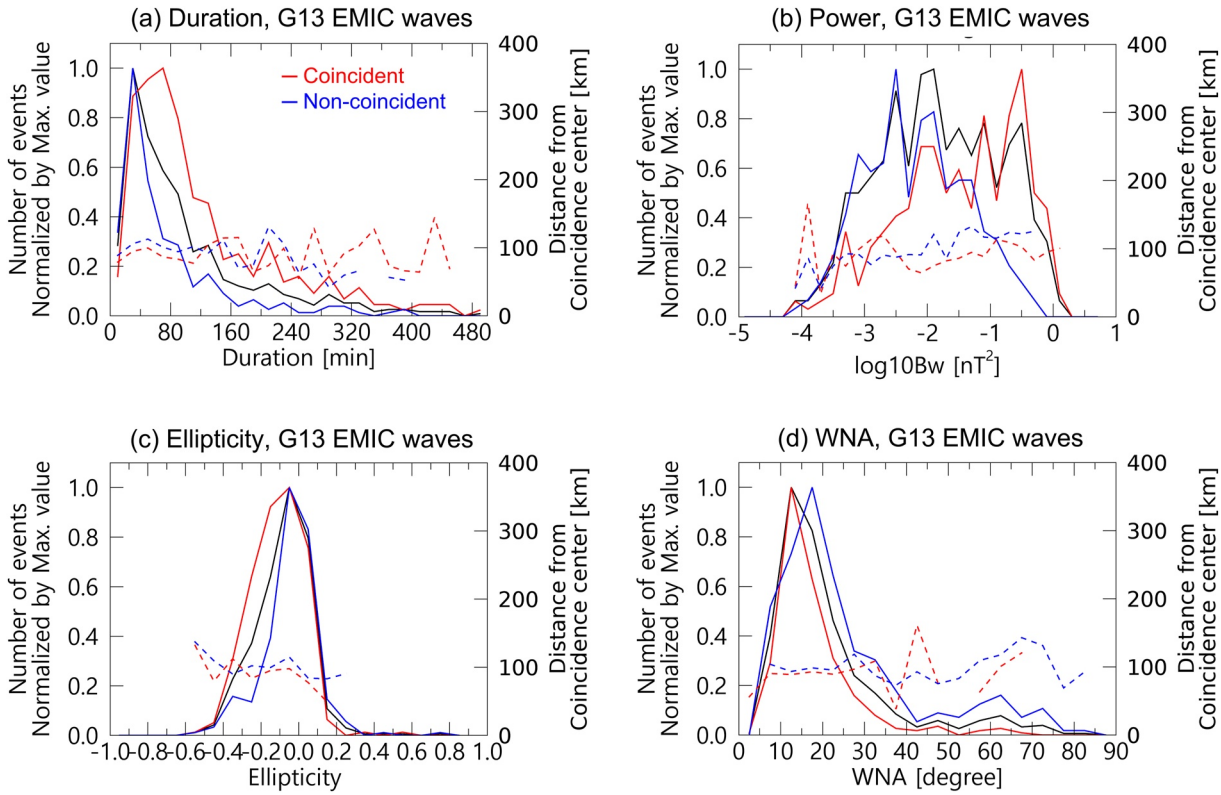

Figure 5. Histograms of the wave properties for coincident (red), non-coincident (blue) events, and total (black) events, (a) duration, (b) amplitude, (c) ellipticity, and (d) wave normal angle.

we selected 32 events that show a clear high-frequency ($f > 0.4$ Hz) transmission to the ground. Figure 6 shows examples of a filtered event and a non-filtered event. Note that both filtered events and non-filtered events are a subset of the coincident group discussed in Section 3.

In Figures 7 and 8, we compare the same variables as used in Section 3. Figure 7 shows the spatial distribution of the filtered and non-filtered events. While the L distribution is relatively similar, the MLT distribution shows a clear difference between the two groups. The non-filtered events are focused on the afternoon sector (12–16 MLT) and the filtered events are located more on the duskside (14–18 MLT) than the non-filtered events. Although the number of events for both groups is not significantly high, a clear MLT difference (well-organized as well) implies that there should be underlying physical processes that produce the wave filtering at high frequencies, when waves propagate from the source region in the magnetosphere to the ground through the ionosphere.

Statistics of the geomagnetic conditions are shown in Figure 8. While the AE and Kp index showed a difference between the coincident and non-coincident groups in Section 3, these geomagnetic indices for the filtered and non-filtered groups do not show statistical differences. Even though the fact that the number of events is not sufficient enough to show a significant level of statistics, the difference in the F10.7 index can be meaningfully interpreted as that the F10.7 index is closely related to the ionospheric plasma density and/or conductivities.

Interestingly, the wave properties show more well-characterized features between the filtered and non-filtered groups than the geomagnetic activities. Figure 9 shows that both ellipticity and wave normal angle are clearly distinguishable between two groups, in contrast to the case for the coincident and non-coincident groups. The ellipticities for the filtered group are statistically more L-mode with an average value of −0.18 than the nonfiltered group which is more linearly polarized. In addition, the wave normal angles for the non-filtered group are slightly higher than those for the filtered group (Figure 9b). Based on these results, we expect that the wave properties at the source region significantly contribute to the frequency-dependent wave propagation to the ground.

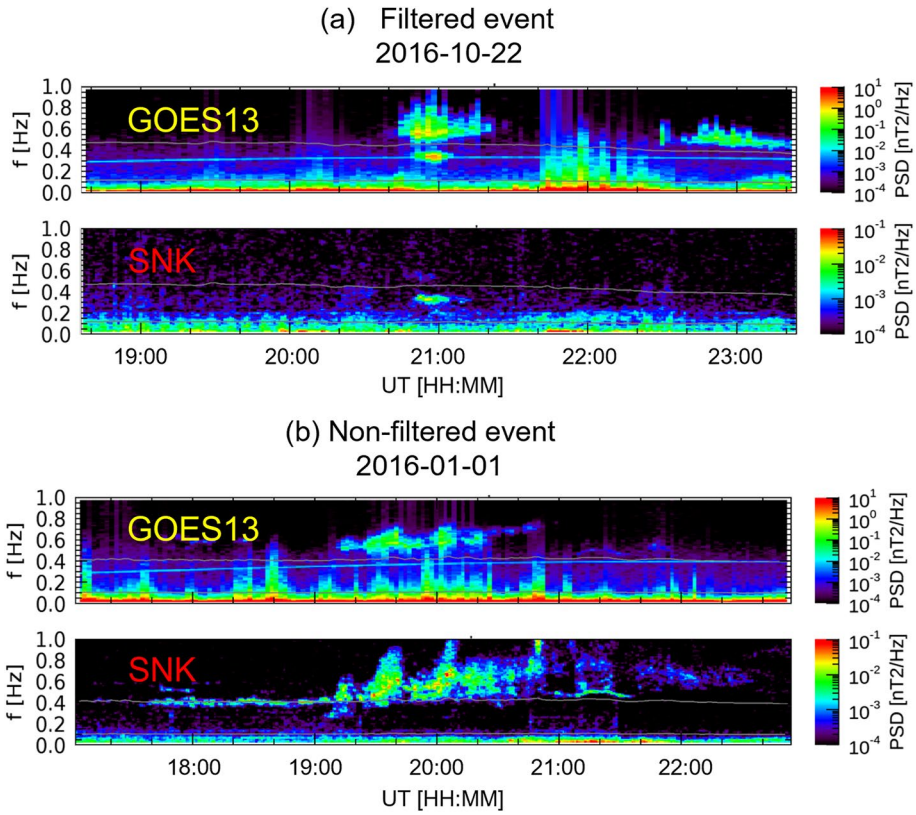

Figure 6. Spectrogram of (a) a filtered event and (b) a non-filtered event. The upper panels show the Geostationary Operational Environment Satellite (GOES) 13 observations and the bottom panels show the SNK observations. The gray curves in each panel indicate the local He^+ gyrofrequency at the GOES 13 location.

In order to estimate the contribution of the ionosphere on the EMIC wave propagation, we also compared the measured vertical total electron content (VTEC) and the altitude profile of the electron density obtained from the international reference ionosphere (IRI-2016) model (Bilitza et al., 2017) at the SNK location. The VTEC maps are available at the Madrigal database (Rideout & Coster, 2006; Vierinen et al., 2015). Figure 10 shows the average VTEC ((a)–(c)) and its standard deviation ((d)–(f)) near the SNK location for the filtered, non-filtered group, and total events, respectively. The average VTEC at the SNK location is higher for the non-filtered group than the filtered group. In addition, the electron profiles from the IRI-2016 support that the non-filtered EMIC waves are more frequently observed in a high ionospheric plasma density environment (See Figure 10g), although

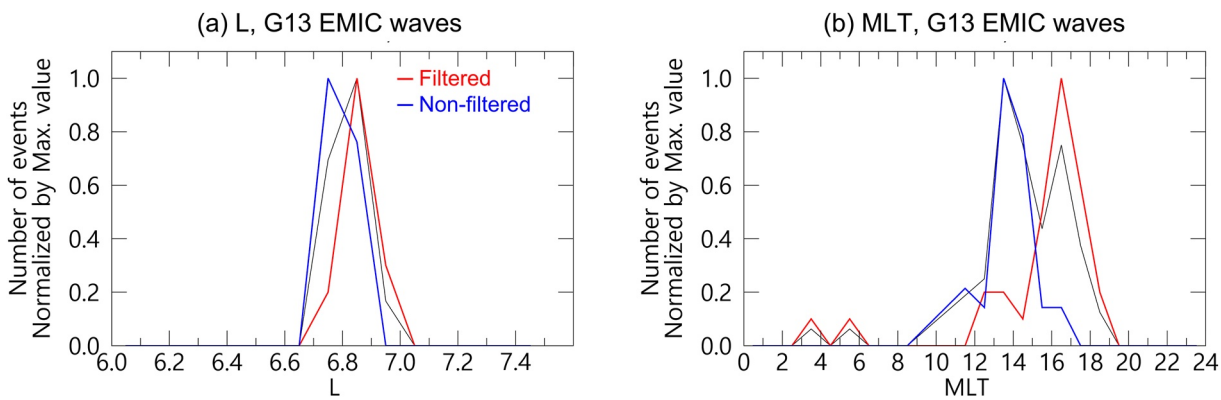

Figure 7. The spatial distribution of Electromagnetic Ion Cyclotron (EMIC) wave events with the same format as Figure 3, but for the filtered events (red), non-filtered events (blue), and total (black) events.

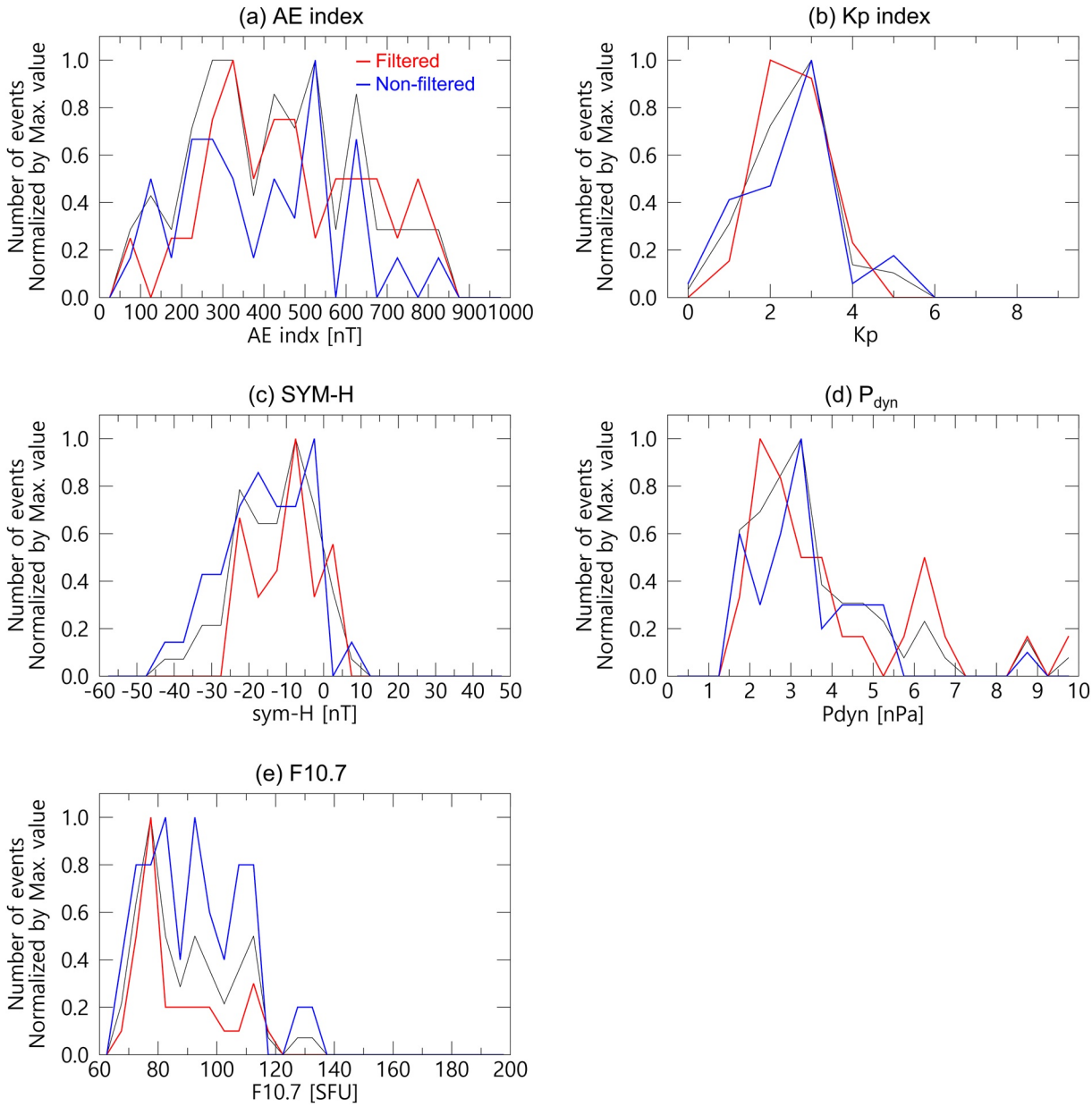

Figure 8. Geomagnetic activity during Electromagnetic Ion Cyclotron (EMIC) wave events with the same format as Figure 4, but for the filtered events (red), non-filtered events (blue), and total (black) events.

the spread of the quartiles indicates that there is considerable overlap in the distributions. The lower standard deviation of VTEC for non-filtered events indicates that most of the non-filtered events statistically have higher VTEC than filtered events. On the other hand, the higher standard deviation for filtered events implies that high-frequency filtering occurs under various VTEC conditions. The fact that non-filtered events tend to be observed under higher electron density seems opposite to the conventional understanding of the relationship between the wave propagation and the ionospheric density; it is usually thought that the higher ionospheric density in the *E* region can trap the waveguide so that the wave propagation along the field line is disturbed (Braysy & Mursula, 2001; Kim & Johnson, 2016; Lessard et al., 2015; Lessard & Knudsen, 2001; Ludlow et al., 1989). However, the ionospheric filtering effect can be extremely complicated by various factors (e.g., perpendicular wave number, ionospheric density profile, wave propagation path, etc.). We further discuss the ionospheric effect on wave filtering in Section 5.

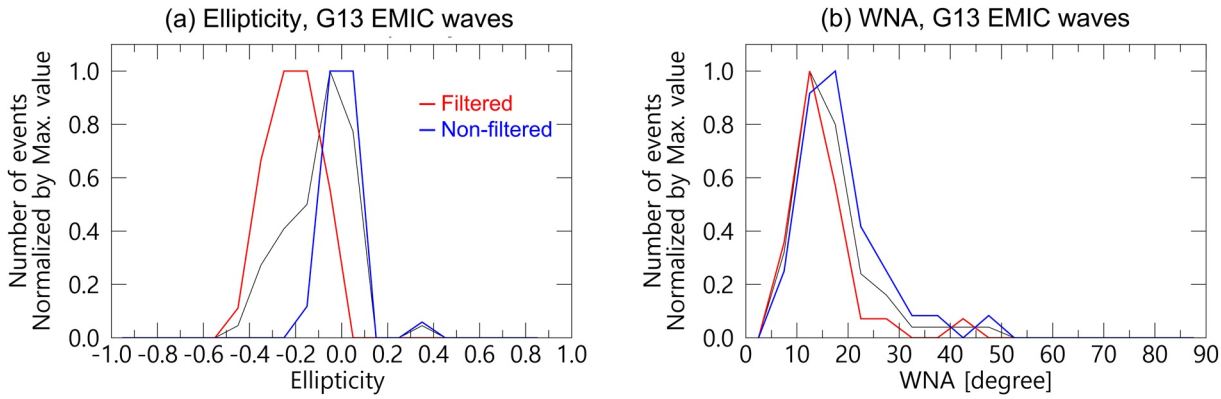

Figure 9. Wave properties of the Electromagnetic Ion Cyclotron (EMIC) wave events with the same format as Figure 5, but for the filtered events (red), non-filtered events (blue), and total (black) events.

5. Summary and Discussion

In this study, we surveyed EMIC waves simultaneously observed in space and at a magnetically conjugate location on the ground. The total observation period was from October 2015 to December 2017. The magnetic conjunction between the geosynchronous orbit satellite and the ground magnetometer provided 24 hr-long and stable conjugate observations of the magnetic field. Consideration for the horizontal ducting effect in the ionosphere was able to be reduced thanks to small differences in L and MLT for the conjugate pair. Our findings are separated into two parts. One is wave coincidence which is introduced in Section 3. Another is the high-frequency wave filtering which is introduced in Section 4.

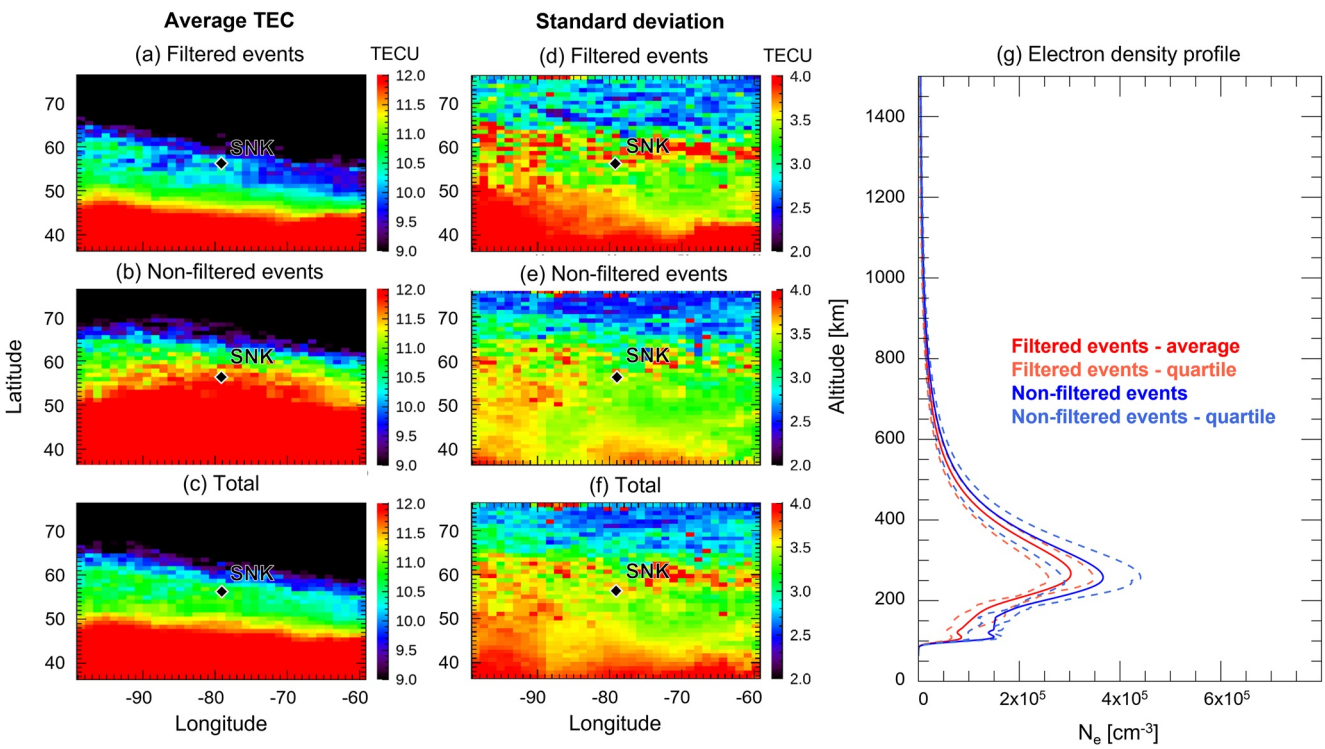

Figure 10. Averaged vertical total electron content map near the SNK station for (a) filtered, (b) non-filtered, and (c) total events. Standard deviation for (d) filtered, (e) non-filtered, and (f) total events. (g) The altitudinal electron density profile for the filtered (red) and non-filtered events (blue) from the international reference ionosphere (IRI-2016) model.

To understand the controlling factors for the coincidence of the wave observations, we investigated the spatial distribution of the waves, geomagnetic activity, and wave properties. The major findings are as follows.

1. The MLT distribution of the coincident group predominantly occurs in the dayside, from noon to dusk. On the other hand, non-coincident events are more evenly distributed.
2. While the SYM-H, solar wind dynamic pressure, and F10.7 index are similar between the coincident and non-coincident groups, the AE and Kp index are higher for the coincident group.
3. The duration and intensity of EMIC waves for the coincident group are statistically higher than those for the non-coincident group, while the polarization characteristics (ellipticity and wave normal angle) are similar.

The coincidence of the waves (whether they can propagate down to the ground or not) is primarily dominated by the wave power and duration. This makes sense assuming the attenuation rate does not significantly change by the other conditions. Then the intensity of the wave on the ground tends to be higher for the high-intensity waves at the source region. Likewise, waves with a longer duration have more chance to be observed on the ground. The AE and Kp index also support this. The AE index is a good proxy of substorm activity which can inject energetic particles into the inner magnetosphere. The Kp index is also a good indicator for enhanced earthward convection (Thomsen, 2004). Consequently, the enhanced proton flux in the inner magnetosphere can be a source of particles that can drive EMIC wave instability. The excitation of EMIC waves is more likely to be expected at the plasmaspheric plume where the injected protons pass through regions of high plasma density (Fraser & Nguyen, 2001; Keika et al., 2013; Meredith et al., 2003; Min et al., 2012; Noh et al., 2021; Summers & Thorne, 2003). It has been known that the intensity of the EMIC wave is higher for the high AE and Kp index intervals and also higher near the plasmaspheric plume (Saikin et al., 2016). Our statistical result of the MLT distribution is consistent with previous reports.

We found that 30 events out of 295 coincident events showed a clear high-frequency wave filtering feature. The cutoff frequency is ∼0.4 Hz which is close to the equatorial He^+ gyrofrequency near geosynchronous orbit. Our comparison of high-frequency filtered wave events with non-filtered wave events reveals several statistical differences as follows.

4. There is a clear MLT difference between the filtered and non-filtered groups. The non-filtered group is focused near noon while the filtered group is located toward the duskside.
5. The F10.7 index is slightly higher for the non-filtered group than the filtered group, although there is no clear difference in the other geomagnetic activity indices between the two groups.
6. The ellipticity for the filtered group is more L-mode than that for the non-filtered group for which the ellipticity is mostly linearly polarized.
7. The wave normal angle is slightly more oblique for the non-filtered group than the filtered group.
8. The VTEC (as well as the altitude profile of the electrons from the IRI-2016) is higher for the non-filtered group than the filtered group.

The statistical characteristics of the filtered and non-filtered groups (summary 4–8) are different from those of the coincident and non-coincident groups (summary 1–3). The coincidence of EMIC waves is related to relatively large-scale characteristics and physically intuitive processes such as wave intensity and duration. On the other hand, the high-frequency filtering of the EMIC wave propagation is affected by more complicated physical processes, for example, the characteristics of the wave polarization and/or the plasma environment along the propagation path.

Previously, Kim and Johnson (2016) simulated the EMIC wave propagation from the magnetic equator to higher latitude where the waves pass through the crossover frequency and the bi-ion frequency. They solved the full wave equation for the L-mode He^+-band EMIC waves in 2D space with a background dipole magnetic field. With this model, they found that the crossover frequency plays an important role in the wave propagation from the equatorial source region to the ground. Consistent with the 1D full-wave simulations (Johnson & Cheng, 1999; Johnson et al., 1995), they showed polarization reversal between L-mode and R-mode EMIC waves and mode

coupling from the guided L-mode to the unguided R-mode occur. Since EMIC waves can be reflected at the bi-ion frequency, the wave tunneling effect between the bi-ion frequency and the heavier ion gyrofrequency is also important. The polarization reversal, mode coupling, and tunneling of the wave sensitively depend on the wave normal angle at the generation region. According to their simulation, waves with a large wave normal angle can propagate further to a higher latitude than waves with a small wave normal angle.

Our finding for the wave normal angle is consistent with the result from Kim and Johnson (2016) in which the non-filtered group has a higher wave normal angle than the filtered group. The difference between the simulation by Kim and Johnson (2016) and our finding is that they modeled only for the He^+-band EMIC wave but our statistical difference basically comes from the H^+-band wave filtering. The major difference between H^+-band and He^+-band wave propagation is that the H^+-band wave goes through mode conversion twice in the H^+, He^+, and O^+ plasmas (since there are two stopbands) while the wave propagates to the higher latitude so that they can be attenuated more than the He^+-band waves. This possibly enhances the statistical difference between the filtered group and non-filtered group, in contrast to the result for the coincident and non-coincident group which is a mixture of H^+ and He^+-band EMIC waves.

In addition to the effect of magnetospheric wave propagation, ionospheric conditions can affect the propagation characteristics. Our finding of statistical differences of the electron density and F10.7 between the filtered and non-filtered groups is possibly associated with ionospheric wave transmission. Fedorov et al. (2018) found that the transmission rate decreases according to the distance from the actual beam incident location. This effect is more obvious for higher frequencies. However, our space-ground conjugate pair allows only small separations (mostly smaller than 100 km, see Figure 1), so the effect of the beam incident location may not be very important for our case. They also revealed that there is a frequency window for the wave transmission and it has an oscillatory signature that is sensitive to the ionospheric conductivity. In their result, the transmission rate can significantly be reduced in higher frequency where the frequency is above 0.5 Hz which is somewhat similar to our findings. However, their simulation was conducted for a different ground location than the SNK station, and the oscillatory signature is sensitive to the ionospheric condition, so it would be necessary to calculate the transmission rate incorporating the location of the SNK station and ionospheric conditions that we found in this study.

Likewise, the high-frequency wave filtering is complicated by both magnetospheric wave-band filtering and ionospheric attenuation, because it is not entirely dominated by one effect. Thus, a quantitative comparison of the contribution between the magnetospheric and ionospheric effects on high-frequency filtering is an important topic for future research.

Data Availability Statement

Access to these data is provided by madrigal network via: http://cedar.openmadrigal.org/. GOES 13 data is available at https://satdat.ngdc.noaa.gov/sem/goes/data/. The induction coil magnetometer data from SNK station is available at HTTP://mirl.unh.edu/ULF/cdf/.

Acknowledgments
The work at the New Jersey Institute of Technology (NJIT) was supported by NSF under grant AGS-2133837, AGS-1547252 and AGS-1602560. The work at Augsburg University was supported by NSF under grant AGS-2013648. The work at Princeton University was supported by NSF under grant AGS1602855. Work at Andrews was supported by AGS2131013. GPS TEC data products and access through the Madrigal distributed data system are provided to the community (http://www.openmadrigal.org) by the Massachusetts Institute of Technology (MIT) under support from US National Science Foundation grant AGS-1952737. Data for TEC processing is provided from the following organizations: UNAVCO, Scripps Orbit and Permanent Array Center, Institut Geographique National, France, International GNSS Service, The Crustal Dynamics Data Information System (CDDIS), National Geodetic Survey, Instituto Brasileiro de Geografia e Estatística, RAMSAC CORS of Instituto Geográfico Nacional de la República Argentina, Arecibo Observatory, Low-Latitude Ionospheric Sensor Network (LISN), Topcon Positioning Systems, Inc., Canadian High Arctic Ionospheric Network, Centro di Ricerche Sismologiche, Système d'Observation du Niveau des Eaux Littorales (SONEL), RENAG: REseau NAtional GPS permanent, GeoNet–the official source of geological hazard information for New Zealand, GNSS Reference Networks, Finnish Meteorological Institute, and SWEPOS–Sweden.

References

Arnoldy, R. L., Lewis, P. B., Jr., & Cahill, L. J., Jr. (1979). Polarization of Pc 1 and IPDP pulsations correlated with particle precipitation. *Journal of Geophysical Research*, *84*(A12), A12. https://doi.org/10.1029/ja084ia12p07091

Bilitza, D., Altadill, D., Truhlik, V., Shubin, V., Galkin, I., Reinisch, B., & Huang, X. (2017). International Reference Ionosphere 2016: From ionospheric climate to real-time weather predictions. *Space Weather*, *15*(2), 418–429. https://doi.org/10.1002/2016SW001593

Blum, L. W., Bonnell, J. W., Agapitov, O., Paulson, K., & Kletzing, C. (2017). EMIC wave scale size in the inner magnetosphere: Observations from the dual Van Allen Probes. *Geophysical Research Letters*, *44*(3), 1227–1233. https://doi.org/10.1002/2016GL072316

Bortnik, J., Cutler, J. W., Dunson, C., & Bleier, T. E. (2007). An automatic wave detection algorithm applied to Pc1 pulsations. *Journal of Geophysical Research*, *112*(A4), A04204. https://doi.org/10.1029/2006JA011900

Braysy, T., & Mursula, K. (2001). Conjugate observations of electromagnetic ion cyclotron waves. *Journal of Geophysical Research*, *106*(A4), 6029–6041. https://doi.org/10.1029/2000ja003009

Chen, L., Thorne, R. M., & Bortnik, J. (2011). The controlling effect of ion temperature on EMIC wave excitation and scattering. *Geophysical Research Letters*, *38*(16), L16109. https://doi.org/10.1029/2011GL048653

Clausen, L. B. N., Baker, J. B. H., Ruohoniemi, J. M., & Singer, H. J. (2011). EMIC waves observed at geosynchronous orbit during solar minimum: Statistics and excitation. *Journal of Geophysical Research*, *116*(A10), A10205. https://doi.org/10.1029/2011JA016823

Cornwall, J. M., Coroniti, F. V., & Thorne, R. M. (1970). Turbulent loss of ring current protons. *Journal of Geophysical Research*, *75*(25), 4699–4709. https://doi.org/10.1029/JA075i025p04699

Engebretson, M. J., Posch, J. L., Capman, N. S. S., Campuzano, N. G., Bělik, P., Allen, R. C., et al. (2018). MMS, Van Allen Probes, GOES 13, and ground-based magnetometer observations of EMIC wave events before, during, and after a modest interplanetary shock. *Journal of Geophysical Research: Space Physics*, *123*(10), 8331–8357. https://doi.org/10.1029/2018JA025984

Fedorov, E. N., Pilipenko, V. A., Engebretson, M. J., & Hartinger, M. D. (2018). Transmission of a magnetospheric Pc1 wave beam through the ionosphere to the ground. *Journal of Geophysical Research: Space Physics*, *123*(5), 3965–3982. https://doi.org/10.1029/2018JA025338

Fraser, B. J., & Nguyen, T. S. (2001). Is the plasmapause a preferred source region of electromagnetic ion cyclotron waves in the magnetosphere. *Journal of Atmospheric and Solar-Terrestrial Physics*, *63*(11), 1225–1247. https://doi.org/10.1016/S1364-6826(00)00225-X

Fujita, S., & Tamao, T. (1988). Duct propagation of hydromagnetic waves in the upper ionosphere 1. Electromagnetic field disturbances in high latitudes associated with localized incidence of a shear alfven wave. *Journal of Geophysical Research*, *93*(A12), 14665–14673. https://doi.org/10.1029/ja093ia12p14665

Greifinger, C., & Greifinger, P. S. (1968). Theory of hydromagnetic propagation in the ionospheric waveguide. *Journal of Geophysical Research*, *73*(23), 23–7490. https://doi.org/10.1029/ja073i023p07473

Hayakawa, M., Shimakura, S., Kobayashi, T., & Sato, N. (1992). A study of polarization of irregular pulsations of diminishing period and their generation mechanism. *Planetary and Space Science*, *40*(8), 1081–1091. https://doi.org/10.1016/0032-0633(92)90037-o

Hu, Y., Denton, R. E., & Johnson, J. R. (2010). Two-dimensional hybrid code simulation of electromagnetic ion cyclotron waves of multi-ion plasmas in a dipole magnetic field. *Journal of Geophysical Research*, *115*(A9), A09218. https://doi.org/10.1029/2009JA015158

Johnson, J. R., Chang, T., & Crew, G. B. (1995). A study of mode conversion in an oxygenhydrogen plasma. *Physics of Plasmas*, *2*(4), 1274–1284. https://doi.org/10.1063/1.871339

Johnson, J. R., & Cheng, C. Z. (1999). Can ion cyclotron waves propagate to the ground? *Geophysical Research Letters*, *26*(6), 671–674. https://doi.org/10.1029/1999gl900074

Jordanova, V. K., Albert, J., & Miyoshi, Y. (2008). Relativistic electron precipitation by EMIC waves from self-consistent global simulations. *Journal of Geophysical Research*, *113*(A3), A00A10. https://doi.org/10.1029/2008JA013239

Keika, K., Takahashi, K., Ukhorskiy, A. Y., & Miyoshi, Y. (2013). Global characteristics of electro-magnetic ion cyclotron waves: Occurrence rate and its storm dependence. *Journal of Geophysical Research*, *118*(7), 4135–4150. https://doi.org/10.1002/jgra.50385

Kim, E.-H., & Johnson, J. R. (2016). Full-wave modeling of EMIC waves near the He^+ gyrofrequency. *Geophysical Research Letters*, *42*(1), 13–21. https://doi.org/10.1002/2015GL066978

Kim, H., Lessard, M. R., Engebretson, M. J., & Luhr, H. (2010). Ducting characteristics of Pc 1 waves at high latitudes on the ground and in space. *Journal of Geophysical Research*, *115*, A9. https://doi.org/10.1029/2010JA015323

Kim, H., Lessard, M. R., Engebretson, M. J., & Young, M. A. (2011). Statistical study of Pc1–2 wave propagation characteristics in the high-latitude ionospheric waveguide. *Journal of Geophysical Research*, *116*, A7. https://doi.org/10.1029/2010JA016355

Kim, H., Schiller, Q., Engebretson, M. J., Noh, S., Kuzichev, I., Lanzerotti, L. J., et al. (2021). Observations of particle loss due to injection-associated electromagnetic ion cyclotron waves. *Journal of Geophysical Research*, *126*(2), e2020JA02850. https://doi.org/10.1029/2020JA028503

Lessard, M. R., & Knudsen, D. J. (2001). Ionospheric reflection of small-scale alfvn waves. *Geophysical Research Letters*, *28*(18), 3573–3576. https://doi.org/10.1029/2000gl012529

Lessard, M. R., Lindgren, E. A., Engebretson, M. J., & Weaver, C. (2015). Solar cycle dependence of ion cyclotron wave frequencies. *Journal of Geophysical Research: Space Physics*, *120*(6), 4711–4718. https://doi.org/10.1002/2014JA020791

Ludlow, G. R., Cornilleau-Wehrlin, N., Hughes, W. J., & Singer, H. J. (1989). Simultaneous observation of a Pc 1 Pulsation by the Air Force Geophysics Laboratory magnetometer network and GEOS 1. *Journal of Geophysical Research*, *94*(A6), 6633–6642. https://doi.org/10.1029/ja094ia06p06633

Ludlow, G. R., Hughes, W. J., Engebretson, M. J., Slavin, J. A., Sugiura, M., & Singer, H. J. (1991). Ion cyclotron waves near L = 4.6: A ground-satellite correlation study. *Journal of Geophysical Research*, *96*(A2), 1451–1466. https://doi.org/10.1029/90ja02005

Mann, I. R., Usanova, M. E., Murphy, K., Robertson, M. T., Milling, D. K., Kale, A., et al. (2014). Spatial localization and ducting of EMIC waves: Van Allen Probes and ground-based observations. *Geophysical Research Letters*, *41*(3), 785–792. https://doi.org/10.1002/2013GL058581

Meredith, N. P., Thorne, R. M., Horne, R. B., Summers, D., Fraser, B. J., & Anderson, R. R. (2003). Statistical analysis of relativistic electron energies for cyclotron resonance with EMIC waves observed on CRRES. *Journal of Geophysical Research*, *108*(A6), 1250. https://doi.org/10.1029/2002JA009700

Min, K., Lee, J., Keika, K., & Li, W. (2012). Global distribution of EMIC waves derived from THEMIS observations. *Journal of Geophysical Research*, *117*(A5), A05219. https://doi.org/10.1029/2012JA017515

Miyoshi, Y., Sakaguchi, K., Shiokawa, K., Evans, D., Albert, J., Connors, M., & Jordanova, V. (2008). Precipitation of radiation belt electrons by EMIC waves, observed from ground and space. *Geophysical Research Letters*, *35*(23), L23101. https://doi.org/10.1029/2008GL035727

Ni, B., Cao, X., Zou, Z., Zhou, C., Gu, X., Bortnik, J., et al. (2015). Resonant scattering of outer zone relativistic electrons by multiband EMIC waves and resultant electron loss time scales. *Journal of Geophysical Research: Space Physics*, *120*(9), 7357–7373. https://doi.org/10.1002/2015JA021466

Noh, S.-J., Lee, D.-Y., Kim, H., Lanzerotti, L. J., Gerrard, A., & Skoug, R. M. (2021). Upper limit of proton anisotropy and its relation to electromagnetic ion cyclotron waves in the inner magnetosphere. *Journal of Geophysical Research: Space Physics*, *126*(5), e2020JA028614. https://doi.org/10.1029/2020JA028614

Perraut, S., Gendrin, R., Roux, A., & de Villedary, C. (1984). Ion cyclotron waves: Direct comparison between ground-based measurements and observations in the source region. *Journal of Geophysical Research*, *89*(A1), 195–202. https://doi.org/10.1029/ja089ia01p00195

Rideout, W., & Coster, A. (2006). Automated GPS processing for global total electron content data. *GPS Solutions*, *10*(3), 219–228. https://doi.org/10.1007/s10291-006-0029-5

Saikin, A. A., Zhang, J.-C., Allen, R. C., Smith, C. W., Kistler, L. M., Spence, H. E., et al. (2015). The occurrence and wave properties of H^+-He^+-and O^+-band EMIC waves observed by the Van Allen Probes. *Journal of Geophysical Research: Space Physics*, *120*(9), 7477–7492. https://doi.org/10.1002/2015JA021358

Saikin, A. A., Zhang, J.-C., Smith, C. W., Spence, H. E., Torbert, R. B., & Kletzing, C. A. (2016). The dependence ongeomagnetic conditions and solar winddynamic pressure of the spatial distribu-tions of EMIC waves observed by the VanAllen Probes. *Journal of Geophysical Research: Space Physics*, *121*(5), 4362–4377. https://doi.org/10.1002/2016JA022523

Shin, J., Kim, K.-H., Jin, H., Kim, H., Kwon, J.-W., Lee, S., et al. (2016). Development of ground-based search-coil magnetometer for near-Earth space research. *Journal of Magnetics*, *21*(4), 509–515. https://doi.org/10.4283/jmag.2016.21.4.509

Singer, H. J., Matheson, L., Grubb, R., Newman, A., & Bouwer, S. D. (1996). *Monitoring space weather with the GOES magnetometers*. In E. R. Washwell (Ed.), *SPIE conference proceedings* (Vol. 2812, pp. 299–308).

Summers, D. (2005). Quasi-linear diffusion coefficients for field-aligned electromagnetic waves with applications to the magnetosphere. *Journal of Geophysical Research*, *110*(A8), A08213. https://doi.org/10.1029/2005JA011159

Summers, D., & Thorne, R. M. (2003). Relativistic electron pitch-angle scattering by electromagnetic ion cyclotron waves during geomagnetic storms. *Journal of Geophysical Research*, *108*(A4), 1143. https://doi.org/10.1029/2002JA009489

Thébault, E., Finlay, C. C., Beggan, C. D., Alken, P., Aubert, J., Barrois, O., et al. (2015). International geomagnetic reference field: The 12th generation. *Earth Planets and Space*, *67*(1), 79. https://doi.org/10.1186/s40623-015-0228-9

Thomsen, M. F. (2004). Why Kp is such a good measure of magnetospheric convection. *Space Weather*, *2*(11), S11004. https://doi.org/10.1029/2004SW000089

Thorne, R. M., & Kennel, C. F. (1971). Relativistic electron precipitation during magnetic storm main phase. *Journal of Geophysical Research*, *76*(19), 4446–4453. https://doi.org/10.1029/JA076i019p04446

Tsyganenko, N. A., & Sitnov, M. I. (2005). Modeling the dynamics of the inner magnetosphere during strong geomagnetic storms. *Journal of Geophysical Research*, *110*(A3), A03208. https://doi.org/10.1029/2004JA010798

Upadhyay, A., Kakad, B., Kakad, A., Omura, Y., & Sinha, A. K. (2020). Occurrence characteristics of electromagnetic ion cyclotron waves at sub-auroral Antarctic station Maitri during solar cycle 24. *Earth Planets and Space*, *72*(1), 35. https://doi.org/10.1186/s40623-020-01157-7

Usanova, M. E., Mann, I. R., Kale, Z. C., Rae, I. J., Sydora, R. D., Sandanger, M., et al. (2010). Conjugate ground and multisatellite observations of compression-related EMIC Pc1 waves and associated proton precipitation. *Journal of Geophysical Research*, *115*(A7), A07208. https://doi.org/10.1029/2009JA014935

Usanova, M. E., Mann, I. R., Rae, I. J., Kale, Z. C., Angelopoulos, V., Bonnell, J. W., et al. (2008). Multipoint observations of magnetospheric compression-related EMIC Pc1 waves by THEMIS and CARISMA. *Geophysical Research Letters*, *35*(17), L17S25. https://doi.org/10.1029/2008GL034458

Vierinen, J., Coster, A. J., Rideout, W. C., Erickson, P. J., & Norberg, J. (2015). Statistical framework for estimating GNSS bias. *Advanced Manufacturing Technology*, *9*(3), 1303–1312. https://doi.org/10.5194/amtd-8-9373-2015